ADVANCED MATERIALS
www.advmat.de

Solid-State Electrolyte Design for Lithium Dendrite Suppression

Xiao Ji, Singyuk Hou, Pengfei Wang, Xinzi He, Nan Piao, Ji Chen, Xiulin Fan, and Chunsheng Wang**

All-solid-state Li metal batteries have attracted extensive attention due to their high safety and high energy density. However, Li dendrite growth in solid-state electrolytes (SSEs) still hinders their application. Current efforts mainly aim to reduce the interfacial resistance, neglecting the intrinsic dendrite-suppression capability of SSEs. Herein, the mechanism for the formation of Li dendrites is investigated, and Li-dendrite-free SSE criteria are reported. To achieve a high dendrite-suppression capability, SSEs should be thermodynamically stable with a high interface energy against Li, and they should have a low electronic conductivity and a high ionic conductivity. A cold-pressed Li_3N–LiF composite is used to validate the Li-dendrite-free design criteria, where the highly ionic conductive Li_3N reduces the Li plating/stripping overpotential, and LiF with high interface energy suppresses dendrites by enhancing the nucleation energy and suppressing the Li penetration into the SSEs. The Li_3N–LiF layer coating on Li_3PS_4 SSE achieves a record-high critical current of >6 mA cm^{-2} even at a high capacity of 6.0 mAh cm^{-2}. The Coulombic efficiency also reaches a record 99% in 150 cycles. The Li_3N–LiF/Li_3PS_4 SSE enables $LiCoO_2$ cathodes to achieve 101.6 mAh g^{-1} for 50 cycles. The design principle opens a new opportunity to develop high-energy all-solid-state Li metal batteries.

Lithium-ion batteries have significantly altered human lives through portable electronics and large-scale energy storage. The energy consumption upgrade, due to fifth-generation (5G) mobile networks, electric vehicles, and in grid-scale stationary energy storage, requires the batteries to have both high energy and safety.[1] In all battery technologies, all-solid-state batteries (ASSBs) can potentially satisfy these requirements by pairing lithium metal and a high-voltage cathode using nonflammable and electrochemically stable solid-state electrolytes (SSEs).[2–4] The reduced reactivity between SSEs and electrodes is expected to decrease the irreversible electrolyte consumption and enhance the device cyclability.[3] More importantly, the high mechanical strength is expected to block the lithium dendrite penetration.[5] The unit transference number of Li-ions in SSEs should prevent concentration gradient-induced Li dendrite growth in SSEs.[6]

However, extensive investigations demonstrated that Li dendrites still easily grow in inorganic SSEs, including Li_3PS_4 (LPS),[7] and $Li_7La_3Zr_2O_{12}$ (LLZO),[8] whatever they are in single crystal,[9] amorphous or multicrystal structures. The SSEs with much higher mechanical strength show even lower dendrite suppression capability than that in conventional organic electrolytes.[10] Both intergranularly[11] and intragranularly Li dendrite growth are found in SSEs.[12] However, the mechanism for Li dendrite growth in SSEs is not fully understood. Hypotheses, such as poor interfacial contact, electronic conductivity of bulk electrolytes, and the presence of the grain boundaries (GBs), are proposed to illustrate the counterintuitive dendrite growth in SSEs.[13] The high interfacial resistance and non-uniformity at Li/SSE interface, introducing by GBs, voids, and cracks, are often blamed to be responsible for the Li dendrite growth in SSEs.[13] However, reduction of the non-uniformity by densifying SSE,[14] amorphous SSE, and single crystal SSE[15] cannot block the Li dendrite growth. In addition, to reduce the interfacial resistance, lithiophilic Au,[16] Al_2O_3,[17] ZnO,[18] Ge,[19] and Li_3N,[20] which bridges the energy gap between Li and SSE, were coated on SSEs and lithiophobic Li_2CO_3 was removed from LLZO surface by polishing and heating.[21] However, Li dendrites still grow in SSEs even though the interface resistance is reduced.[22,23]

In sharp contrast to lithiophilic coating and enhancement of the uniformity of SSEs, herein, we design a lithiophobic porous SSE that has a high interface energy against Li, a high ionic conductivity and low electronic conductivity to enhance the dendrite suppression capability. Based on the total energy analyses, we established dendrite suppression criterion: the electrolytes or formed interphases should: 1) be electrochemically stable with Li; 2) have a high ionic conductivity and a low electronic conductivity; and 3) have a high interface energy against Li to suppress Li nucleation and growth inside electrolytes. Li_3N has a high ion conductivity and is stable with Li metal. However,

Dr. X. Ji, S. Hou, Dr. P. Wang, X. He, Dr. N. Piao, Dr. J. Chen, Dr. X. Fan, Prof. C. Wang
Department of Chemical and Biomolecular Engineering
University of Maryland
College Park, MD 20742, USA
E-mail: fxiulin85@gmail.com; cswang@umd.edu
Prof. C. Wang
Department of Chemistry and Biochemistry
University of Maryland
College Park, MD 20742, USA
The ORCID identification number(s) for the author(s) of this article can be found under https://doi.org/10.1002/adma.202002741.

DOI: 10.1002/adma.202002741

simply coating Li_3N on SSE cannot effectively suppress Li dendrites[20] due to the low interface energy of Li_3N against Li. LiF is not only stable with Li but also has a high interface energy against Li and a very low electronic conductivity. LiF SEI coating on SSEs has significantly suppressed Li dendrite growth.[24–26] However, the low ionic conductivity of LiF also enhance the Li plating/stripping overpotential. An Li_3N–LiF composite electrolyte, inheriting the merits of both Li_3N and LiF, can satisfy all the requirement for Li-dendrite-free electrolytes. Li_3N–LiF composite electrolyte is stable against Li metal and has high ionic conductivity, low electronic conductivity, and high interface energy. Therefore, cold-pressed Li_3N–LiF electrolyte was selected as a model electrolyte to demonstrate the Li dendrite suppression principles. In cold-pressed Li_3N–LiF electrolyte, the 3D pores in Li_3N–LiF electrolytes can act as reservoir for plated Li, enlarging the contact area and releasing the interfacial stress during cycles, so the SSEs is not fractured during cycling. The Li penetration depth is controlled by the force balance between Li plating pressure and interfacial tension of LiF to Li. The Li_3N–LiF protected LPS electrolytes achieved a critical current density of over 6 mA cm^{-2} with the high capacity of 6 mAh cm^{-2} at room temperature.

The Li dendrite nucleation and growth in SSEs depend on the energy landscape for Li deposition and stripping inside SSEs, which can be presented by the Butler–Volmer model (**Figure 1**a). The parabolas on the left designates reaction coordinate of Li deposition ($Li^+ + e^- \rightarrow Li$) and the parabolas on the right designates that of Li stripping ($Li \rightarrow Li^+ + e^-$). Before the overpotential is applied, the equilibrium state can be illustrated by the blue lines. Once a potential (η) applied for plating, the energy barrier for Li plating inside electrolyte ($\Delta G'_{Li^+ + e \rightarrow Li}$) decrease while the energy barrier for the Li stripping ($\Delta G'_{Li \rightarrow Li^+ + e}$) increase. When the potential shift reaches the critical overpotential (η^*), the activation energy of Li plating equals to that of Li stripping in SSEs (red dash lines in Figure 1a). Li dendrites will form in SSE when the applied potential is larger than η^*. Here, the η^* can be used as a parameter to evaluate the dendrite suppression capability of a SSE. To improve the η^*, as analyzed by the detailed Butler–Volmer model (Note S1 and Figure S1, Supporting Information), the stability, mechanical properties, and interface energy of the SSE should be enhance to improve the anti-interference ability. The electronic conductivity and the interface resistance should be reduced to decrease the potential applied on the SSEs.

The impact of thermodynamic stability, interface energy, and electronic conductivity of SSEs on the Li dendrite formation is detailed in Figure 1b. When a SSE is stable with Li, electronic insulated, and has low interface energy, Li dendrites grow from Li anode into GBs or pores of SSEs through mechanical Li infiltration due to the high interface tension and Li plating pressure. The mechanical Li dendrite growth mainly contributes to the intergranular growth, such as propagation in GBs, pores, and cracks induced by Li growth (first row in Figure 1b). However, if the local electronic conductivity of SSEs is high, the atomic Li electrochemical potential in SSEs will drop to a potential similar to the Li plating anode, so Li can even directly nucleate and grow inside SSE. (second row in Figure 1b). Only if the SSEs are stable with Li have high interface energy against Li and insulated electronic conductivity, Li dendrites will not nucleate and grow inside SSEs, and not penetrate into SSEs because the high interface energy significantly increases the energy barrier of homogeneous nucleation, and the high interface tension between SSEs and Li also suppresses Li propagation and penetration into SSEs (third row in Figure 1b). For the case that SSEs are unstable with Li, and the formed interphases have a high electronic conductivity, the electrochemical reaction between Li and SSE accelerates the Li dendrite nucleation and growth in SSEs. The Li dendrite growth in SSEs changes from a mechanical pattern to an electrochemical–mechanical pattern (fourth row in Figure 1b).

The interface energy of SSE against Li is the most critical property for SSEs in additional to the high ionic conductivity and low electronic conductivity. The high interface energy of SSE can prevent the Li nuclear inside SSE and Li penetration into SSEs even if SSEs have a high porosity. Since the most highly ionic conductivity electrolytes are not stable with Li, interphases will generate because of the chemical reaction. If the formed the interphases have a high interface energy with Li, the SEI still can suppress the Li dendrite nucleation and growth. However, if

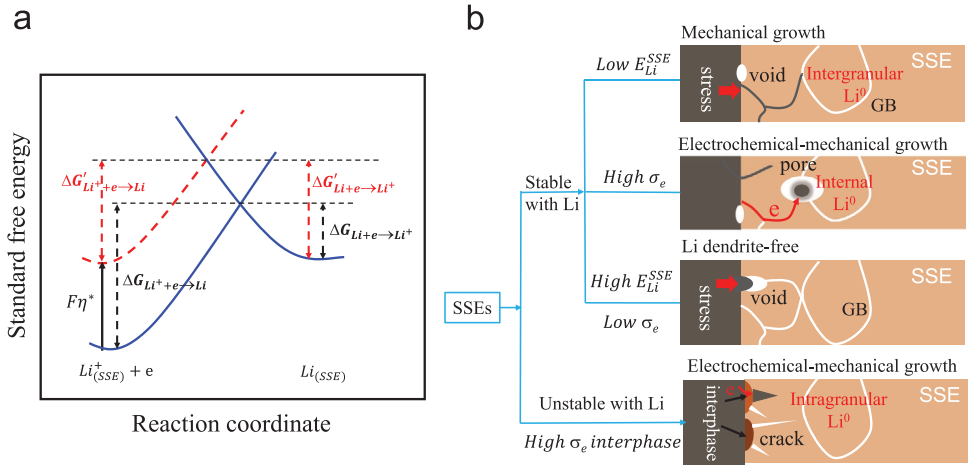

Figure 1. Li dendrite formation mechanism in SSEs. a) Illustration of Butler–Volmer model for Li plating in SSE; b) Li dendrite formation and growth mechanism in SSE with different properties. ΔG, σ_e, and E_{Li}^{SSE} are the activation energies, electronic conductivity, and interface energy between Li and SSEs.

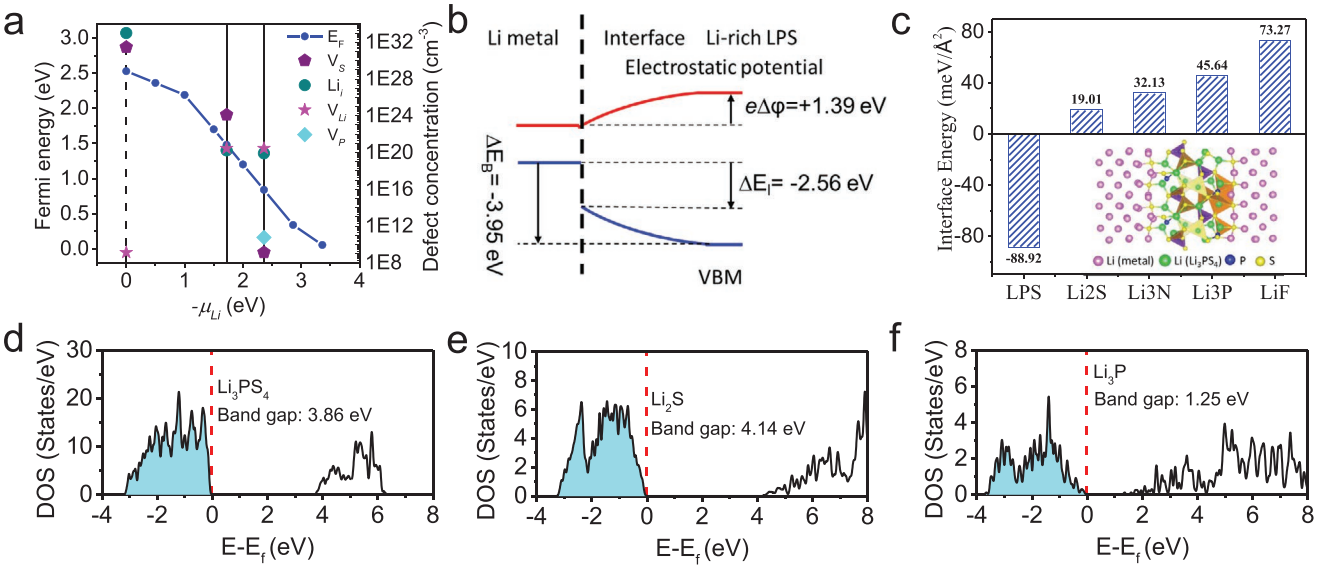

Figure 2. DFT calculations on chemical decomposition of Li metal and LPS SSE interface. a) Fermi level reference to valence band maximum (VBM) determined by charge neutrality at 300 K and defect concentration as a function of Li chemical potential. b) Schematic of the electrostatic potential (red) and VBM (blue) at the Li/LPS interface; details are in Table S1, Supporting Information. c) DFT calculated interface energies and relaxed Li/LPS interface (inset). Color code: purple, Li atoms from metal; green, Li atoms from LPS; blue, P atoms; yellow, S atoms. d–f) The density of states (DOS) and HSE06 bandgap for LPS (d), Li_2S (e), and Li_3P (f). The Fermi levels are set to be 0 eV (red dash lines).

the SEI has a low interface energy and high electronic conductivity, the SEI will accelerate the Li dendrite growth.

Taking the typical LPS electrolyte as an example, we analyzed the electrochemical stability of LPS, electronic conductivity, and the interface energy of the formed SEI against Li by using the first-principles calculations based on density functional theory (DFT) (Figures S2 and S3, Supporting Information).[27] The stability window of LPS is indicated by the solid vertical lines in **Figure 2**a. Figure 2a also shows the Fermi level determined by the charge neutrality at 300 K and defect concentration as the function of the Li chemical potential (μ). Li vacancies (V_{Li}) and Li interstitials (Li_i) are the main intrinsic defects with similar concentrations that suggest Li vacancies and interstitials are perceived as the mobile charger species. As the Li chemical potential reaches to 0.0 eV, which is consistent with the situation that LPS contacts to Li metal. The increase in concentration of S vacancy indicates that the PS_4 anion framework fails. The high S vacancy (V_S) concentration as charge carriers denies the unit transference number at the interface region. As the Li chemical potential increases, the Fermi level increases because the defects create additional states in the bandgap. The upshift of the Fermi level as μ increases demonstrates that more electrons can migrate and cumulate in the LPS SSEs, increasing the electronic conductivity. The energy diagram (Figure 2b) between the Li metal and LPS interface has been calculated to show the charge space region. The electrostatic potential difference (φ_{Li}^{SSE}) at the interface is proposed to be 1.39 V which is considered as a large driving force for the redistribution of charge carries, decomposing the LPS. Moreover, the decomposition is also validated by the DFT relaxed Li/LPS interface as shown in Figure 2b.

The electronic conductivity of LPS and the decomposed products was evaluated by calculating the density of states (DOS). According to the thermodynamic phase diagram (Figure S4, Supporting Information) and experimental results,[28] the decomposition products of LPS are Li_2S and Li_3P. The DOS of LPS, Li_2S, and Li_3P are shown in Figures 2d–f, respectively. LPS and Li_2S can be treated as electronic insulator for their large bandgaps of 3.86 and 4.14 eV. However, the small bandgap (1.25 eV) of Li_3P crystal indicates its electronic semiconductor characteristic. At the electron leakage site, the chemical potential of Li atom in SEI layer $\mu_{Li}^{SEI} = 0$ (Figure S5, Supporting Information). The mess spatial distribution of the reduction products will lead to electric field distribution (Figure S6, Supporting Information), making $\mu_{Li}^{SEI} > 0$ with the applied external circuit. The reduction reaction also leads to volume change, thus introducing cracks in the SSE layer. The reaction induced cracks will also provide opportunity for physical Li dendrite formation pattern.

The interface energies of LPS, Li_2S, and Li_3P against Li metal are shown in Figure 2c. The negative interface energy (–88.92 eV A^{-2}) indicates the spontaneous chemical reaction between Li and LPS. The P-S tetrahedron breaks and S atoms migrate to the surface, re-bonding with the Li atoms from Li metal (Figure 2c inset). The low interface energy of Li_2S against Li metal (19.01 eV Å m^{-2}) indicates its low capability in blocking Li dendrite growth. Li_3P has a higher interface energy than Li_2S, but its interface energy is much lower than LiF. In addition, the high electronic conductivity of Li_3P also promotes Li dendrite growth although it also reduces the applied overpotential.

Based on the DFT results, the challenges for LPS electrolytes are not stable with Li, the decomposed product of Li_2S has a low interface energy against Li. Even worse, Li_3P has a high electronic conductivity. Since the operation temperature is much higher than the zero temperature (K), the decomposition of the SSEs would be accelerated and the electronic conductivity would be enhanced, promoting the dendrite growth. Therefore, the reduction of LPS will self-amplify Li dendrite

growth in each cycle and result in an avalanche breakdown of the cell.

Based on the design principles, the Li/SSE interface should satisfy the following requirements for Li dendrite suppression: 1) be stable with Li metal; 2) has a high interface energy against Li metal to restrict the Li growth into SSEs; 3) has a high ionic conductivity and insulated electronic conductivity. If the SSEs are not stable against Li metal, but the formed interphases satisfy the above requirements, the interphases can also suppress the Li dendrites that penetrate the SSEs. Hence, cold-pressed Li_3N and LiF composite was chosen as a dendrite-free SSE. Both Li_3N and LiF are thermodynamically stable against Li metal. The high ionic conductivity of Li_3N ensures the low overpotential,[29] thus it is selected as a based electrolyte. The interface energy (32.13 meV $Å^{-2}$) of Li_3N is higher than that of Li_2S (Figure 2c; Figure S7, Supporting Information). To further increase the Li dendrite suppression capability, LiF with a high interface energy with Li metal and extremely low electronic conductivity is mixed into Li_3N powder. Moreover, a small amount (≈2% weight ratio) of poly(tetrafluoroethylene) (PTFE) is added to improve the cold-press deformability and the density of the SSE. Since Li_3N will be decomposed at potential above 0.45 V, LPS SSE is used as protect layer to block oxidation reaction from the cathode, while Li_3N–LiF layer can prevent the Li dendrite penetration into LPS. The Li_3N–LiF electrolytes powders were synthesized by mechanical milling of β-Li_3N, LiF, and PTFE. X-ray diffraction (XRD) confirms that the ball-milled Li_3N–LiF powder consists of β-Li_3N, LiF and PTFE (Figure S8, Supporting Information).

The dendrite suppression ability of Li_3N–LiF layer was evaluated at room temperature in symmetric Li/Li_3N–LiF/Li cells by gradually increasing currents from 0.3 to 3.0 mA cm^{-2}, but fixing a capacity of 0.3 mAh cm^{-2}. Li/Li_3N–LiF/Li cells experience activation process due to the high interface energy to Li. Figure S9, Supporting Information, shows the voltage profiles Li/Li_3N–LiF/Li cell during Li plating and stripping cycles after activation cycles. No short-circuit is observed from the voltage profiles Li/Li_3N–LiF/Li cell during Li plating and stripping cycles even at a high current density of 3 mA cm^{-2}. For practical application, a layer of LPS was coated on one side of Li_3N–LiF electrolyte. Therefore, the Li dendrite suppression capability for Li_3N–LiF electrolyte was also evaluated by sandwich Li_3N–LiF on both sides of LPS to form a Li_3N–LiF/LPS/Li_3N–LiF three-layer composite electrolyte. Li_3N and LiF molar ratio of 3:1 is selected to show the dendrite suppression capability of Li_3N–LiF composite since it has a decent balance of ionic conductivity and interface energy as demonstrated by the fast activation process and low overpotentials (Figure S10, Supporting Information). **Figure 3**a shows the voltage profiles of Li/Li_3N–LiF/LPS/Li_3N–LiF/Li symmetric cell during Li plating and stripping with

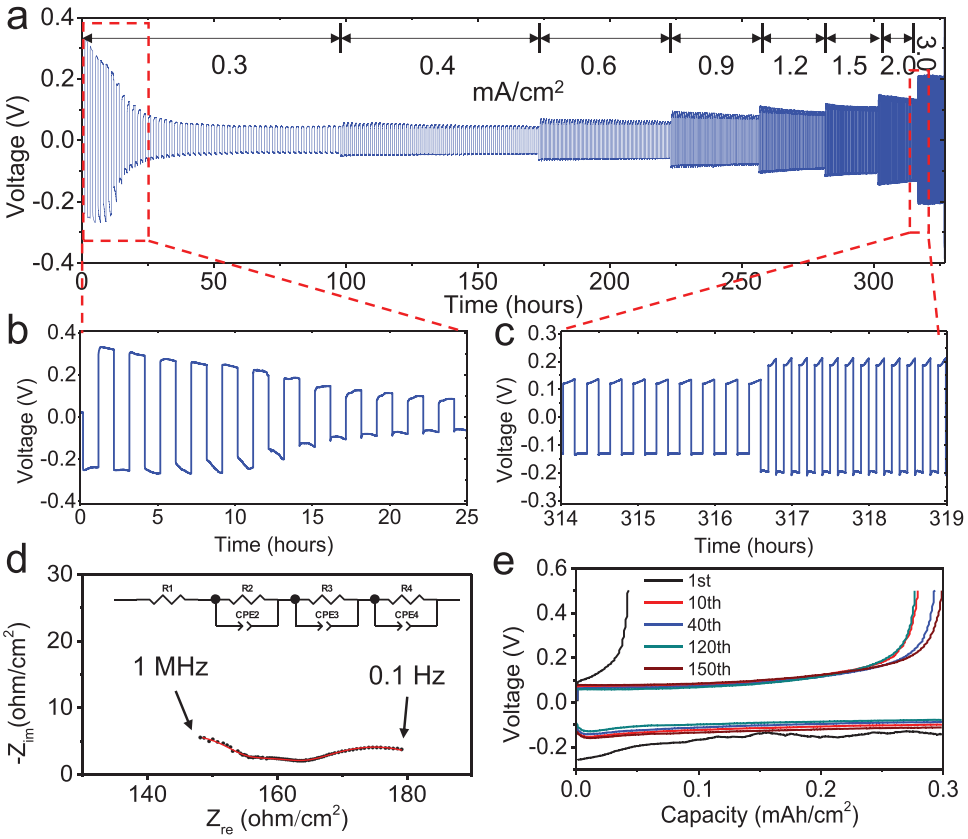

Figure 3. Electrochemical performances of the Li plating/stripping in the Li/Li_3N–LiF/LPS/Li_3N–LiF/Li cell at room temperature. a) Voltage profiles in the symmetric cell at increased current densities with constant capacity of 0.3 mAh cm^{-2}. The details indicated by the areas marked by the red dashes are shown in (b) and (c). d) EIS plot (black dots) and fitted line (red) using the equivalent circuit after cycling at current density of 0.3 mA cm^{-2}. e) Li plating/stripping CEs in Li/Li_3N–LiF/LPS/Li_3N–LiF/SS cell with a current density of 0.3 mA cm^{-2} and voltage cut-off of 0.5 V.

an increasing current density from 0.3 to 3.0 mA cm^{-2} at a fixed capacity of 0.3 mAh cm^{-2}. Same as in Li/Li_3N–LiF/Li cells, an activation process can be observed from the voltage profiles at a current of 0.3 mA cm^{-2}, where the voltage gradually decreases in the first 20 cycles from about 300 to 50 mV and then stay stable (Figure 3b). This activation phenomenon is common observed in the solid state symmetric cell if interface energy is high.[18] The gradual decrease in the voltage of Li/Li_3N–LiF/LPS/Li_3N–LiF/Li cells can be attributed to the increase of specific contact area of the interface and the decrease of real electrolyte thickness result from Li penetration into the voids of Li_3N–LiF layer. The steady voltage profiles reach after 20 cycles suggest that Li will not further grow and penetrate into the SSE under current density of 0.3 mA cm^{-2} due to high interface energy of LiF. As the current density increases, the increase in Li plating and stripping voltage follows ohm's law. Even at a current density of 3.0 mA cm^{-2}, which is more than 3 times higher than the reported critical current density of LPS SSE (0.5 to 1.0 mA cm^{-2}),[30] no abrupt drop of voltage can be observed during the cycling, indicating that no Li dendrites penetrate through the SSE at such a high current density (Figure 3c). The impedance of Li/Li_3N–LiF/LPS/Li_3N–LiF/Li cell after cycle at the current of 0.3 mA cm^{-2} and capacity of 0.3 mAh cm^{-2} for 40 h is shown in Figure 3d. The activated Li/Li_3N–LiF/LPS/Li_3N–LiF/Li cell shows total resistance of about 178 Ω cm^{-2}, in agreement with the calculated value of 180 Ω cm^{-2} from the voltage profile. The fitting line is highly matched with the electrochemical impedance spectroscopy (EIS) plot with the total resistance ($R_1 + R_2$) of the SSE is fitted to be 155.2 Ω cm^{-2} while the two interface resistances for Li|Li_3N–LiF and Li_3N–LiF|LPS interface are fitted to be 15.3 and 12.9 Ω cm^{-2}. The Li plating/stripping Coulombic efficiency (CE) of Li_3N–LiF is evaluated using a Li/Li_3N–LiF/LPS/Li_3N–LiF/SS (SS = stainless steel) half-cell. Figure 3e shows Li plating/stripping voltage profiles of Li/Li_3N–LiF/LPS/Li_3N–LiF/SS half-cell at the current density of 0.3 mA cm^{-2} with cut-off voltage of 0.5 V. The CE for the first Li plating and stripping of Li/Li_3N–LiF/LPS/Li_3N–LiF/SS half-cell is only 11%. The low CE in the first Li plating/stripping may be attributed to the reduction of oxides and impurity on Li_3N–LiF and SS surfaces, which are irreversible. Some platted Li metal may trap in the pores of the Li_3N–LiF surface, which also contributes to the low CE for the first cycle. After a small amount of Li fills into Li_3N–LiF layer after ten activation cycles, the Li plating overpotential decreases due to the increases in the contact area. The CE of half-cell increases to 93% at 10 cycles, and reaches to of 99% after 150th cycle. The high CE demonstrates that Li/Li_3N–LiF interface is highly thermodynamically stable system with high capability to suppress Li dendrite.

The long cycle stability of Li/Li_3N–LiF/LPS/Li_3N–LiF/Li cell at a high and fixed current of 1.0 mA cm^{-2} and capacity of 1.0 mAh cm^{-2} is shown in **Figure 4**a. The voltage profile is stable and no sudden voltage drop of short circuit is observed even

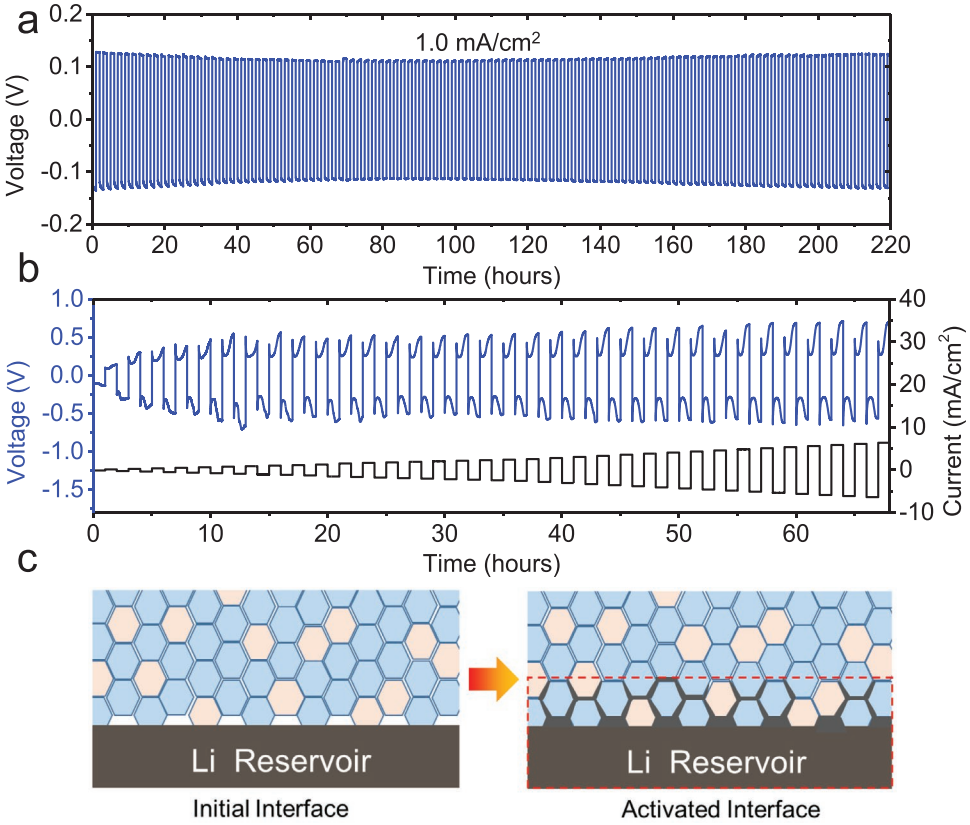

Figure 4. Voltage profile of the Li plating/stripping for large current density. a,b) Voltage profiles of the symmetric cell at current density of 1.0 mA cm^{-2} (a) and step-increased current densities and capacity (b) (fixed 1 h time for Li plating/stripping). c) Scheme for the activation process at the interface, the red dashed line indicates the new interface after the activation process.

after 220 h of Li plating/stripping cycles. The EIS after 220 h of cycles in Figure S11, Supporting Information shows a low impedance of 112 Ω cm^{-2}. The impedance is slightly smaller than that cycled at 0.3 mAh cm^{-2} (Figure 3b), indicating that the increased stress at a high Li-plating/stripping capacity push more Li metal into the Li_3N–LiF layer increasing the interfacial contact at Li/Li_3N–LiF. More aggressive protocol of step-increasing of the current densities but fixed plating and stripping time of 1.0 h was conducted for the Li/Li_3N–LiF/LPS/Li_3N–LiF/Li symmetric cell. As shown in Figure 4b, no short circuit during the cycling is observed even at a high current of 6 mA cm^{-2} and capacity of 6 mAh cm^{-2}. The lower increase in voltage with current density than by ohm's law after 12 h of cycles is mainly attributed to increase the Li penetration into the Li_3N–LiF layer at a high capacity. The gradually increased Li plating capacity in each cycles increase the force to drive more plated Li into the pores of Li_3N–LiF layer, as illustrated in Figure 4c. However, the high interface energy of Li_3N–LiF generates a large opposite force to balance the increased pressure from plated Li plating, and prevent the Li dendrite amplification. The intergranular pores serve as 3D Li reservoir, releasing stress for Li plating on the anode rather than SSEs. Even with thinner 500 μm Li_3N–LiF/LPS SSE, the Li_3N–LiF layer (100 μm) show a high dendrite suppression capability (Figure S12, Supporting Information). In sharp contrast, the Li/LPS/Li cell exhibits a much low critical current density of 0.4 mA cm^{-2} under the same testing protocol (Figure S13, Supporting Information). The results clearly demonstrate that the Li_3N–LiF layer between Li and LPS SSE can significantly suppress the Li dendrite propagation through the SSE, increasing the critical current density by 15 times. The electrochemical performance of Li/Li_3N/LPS/Li_3N/Li cell at increased current from 0.3 to 3.0 mA cm^{-2} but fixed capacity of 0.3 mAh cm^{-2} is also demonstrated in Figure S14, Supporting Information. The results indicate that the introduction of LiF into Li_3N enhanced the capability in suppressing Li dendrite penetration, especially for high-energy capacity case.

The interface morphology, structure, and composition of Li/Li_3N–LiF/LPS electrolyte before and after Li plating/stripping cycles were analyzed using scanning electron microscopy (SEM), and X-ray photoelectron spectroscopy (XPS). **Figure 5**a shows the cross section of the Li_3N–LiF/LPS electrolytes. The Li_3N–LiF and LPS interface is intimate contacted as indicated by the red dash line. The thickness for the Li_3N–LiF layer is measured to be about 200 μm while the LPS layer is about 800 μm. The surface morphology of the Li_3N–LiF layer before and after Li plating/stripping cycles are shown in Figures 5b,c, respectively. Before cycling, the surface shows substantial voids with the size distribution ranging from 1 μm to nano-scales. The voids reduce the contact area between Li and Li_3N–LiF layer leading to a high Li-plating/stripping overpotential in the first cycles. After activation cycles, the voids in Li_3N–LiF was filled by Li and the surface becomes smooth. The porous structure of cold-pressed Li_3N–LiF provides room for plated Li to release the interfacial stress and increases the interface area. The surface compositions of Li_3N–LiF and LPS after fully Li stripping were analyzed with the binding energies (284.6 eV) of C 1s as reference. Figure 5d shows the XPS analysis of cycled Li_3N–LiF surface. A N 1s spectra at the binding energy of 396.9 eV corresponds to the pure Li_3N XPS results.[13] From F1s spectra, a typical LiF peak was detected at the binding energy of 684.8 eV (Figure 5e). The XPS results confirm that the Li/Li_3N–LiF interface is side reaction free. The XPS of Li_3N–LiF protected LPS shows P 2p spectra with doublet peaks of 2p3/2 (132.5 eV) (Figure 5f) and 2p1/2 (131.6 eV) and S2p spectra (Figure S15, Supporting Information), indicating that the no LPS was reduced during the cycling process[31] and the LPS was well protected from being reduced during the cycling process.

The Li penetration depth into Li/Li_3N–LiF was analyzed using time-of-flight secondary-ion mass spectrometry (ToF-SIMS) after 50 Li plating/stripping cycles at a constant current of 1.0 mA cm^{-2} and capacity of 1 mAh cm^{-2}. The side view of the sputtered carter (inset) for the Li depth profile is shown in Figure 5g and Figure S16, Supporting Information. Strong signals for lithium were found within the topmost layer. As the depth increase, the content of lithium significantly decreases and becomes steady at the depth about 8 μm. The Li depth profile supports that lithium is trapped into the pores of the Li_3N–LiF layer after cycling, in consistent with the electrochemical results (Figure 3a) and SEM images (Figure 4c). The top view of the spatial distribution of lithium at the depth of 0.91and 11.82 μm is shown in Figures 5h and 5f, respectively. The red area indicates the cumulated lithium in the Li_3N–LiF sub-surface layer at 0.91 μm, suggesting that lithium metal is trapped in the particle boundaries of Li_3N and LiF. A large amount of lithium metal localized in the particles boundaries significantly enhances the contact area thus decreasing the Li plating/stripping voltage. As the sputter depth increases to 11.82 μm, the blue area which indicates the Li concentration significantly decreased. The Li metal disperses at the depth of 11.82 μm. The Li only penetrated into 8 μm of Li_3N–LiF layer, which is much smaller than the thickness of Li_3N–LiF layer (≈200 μm). As stated early, the limited Li penetration thickness into Li_3N–LiF layer is attributed to a high interface energy of Li_3N–LiF against Li, which increases with penetration thickness.

As aforementioned, cold-pressed Li_3N–LiF is used as a model electrolyte to demonstrate the Li dendrite suppression criteria, in which interface energy and thermodynamic stability of SSEs is more critical than the electronic conductivity. It is also possible to use a mixed conductive layer that is stable with Li and has a very high interface energy with Li to protect LPS or LLZO from the Li dendrites.[32] The high interface energy of mixed conductive layer prevents Li deposition in the mixed conductive layer, so the Li will not directly contact with LPS or LLZO and cannot penetrate into the SSEs. In addition, since the mixed conductive layer is stable with LPS (or LLZO), a potential drop exists at the interface between the mixed conductive layer and LPS (or LLZO), which can avoid the LPS (or LLZO) potential to drop to the Li plating potential thus preventing the Li nucleation inside SSE.

The electrochemical performance of Li/Li_3N–LiF/LPS/LCO full cells (Figure S17, Supporting Information) with the lithium cobalt oxide (LCO) areal capacity of about 1.0 mAh cm^{-2} was evaluated at a current of 0.3 mA cm^{-2}. **Figure 6** shows the charge/discharge curves of Li/Li_3N–LiF/LPS/LCO cell at the current density of 0.3 mA cm^{-2} between 2.7 and 3.8 V at room temperature. The Li/Li_3N–LiF/LPS/LCO provides a charge capacity of 128.9 mAh g^{-1} and discharge capacity of 101.3 mAh g^{-1} in the first

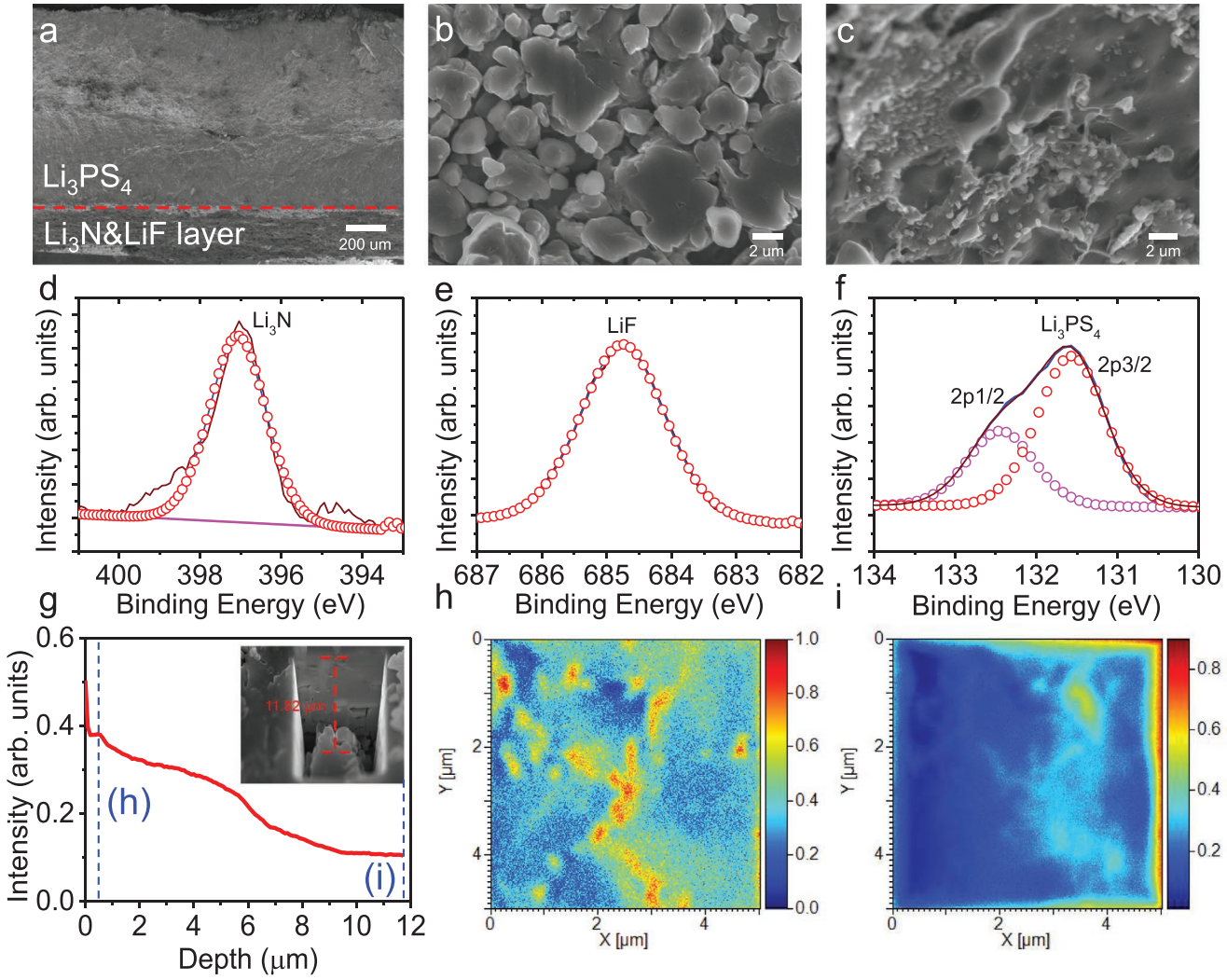

Figure 5. a–c) Surface analyses for the Li/Li_3N–LiF interface. a) Side view of the layered structure of Li_3N–LiF/LPS electrolytes. b,c) SEM images of the Li_3N–LiF surface before (b) and after (c) 50 cycles. d–f) High-resolution XPS N 1s (d), F 1s (e), and P 2p (f) spectra of the Li/Li_3N–LiF and Li_3N–LiF/LPS interfaces. g–i) ToF-SIMS analysis for the lithium element distribution in the Li_3N–LiF layer after cycling at constant capacity of 1 mAh cm^{-2}. g) Depth profiling of spatial distribution of Li element and SEM image (inset) for the Ga^+ ion beam sputtered crater. h,i) Top views of the Li element distribution at depths of 0.91 (h) and 11.82 μm (i).

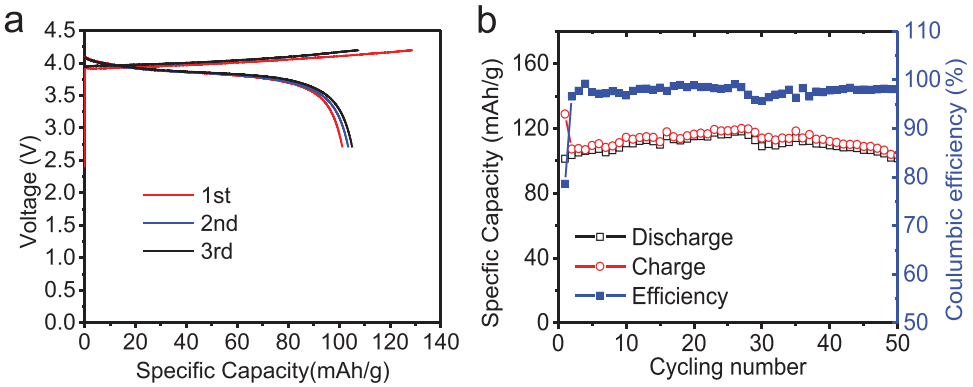

Figure 6. Electrochemical performance of Li/Li_3N–LiF/LPS/LCO cell. a) Charge/discharge curves in different cycles at 0.3 mA cm^{-2} at room temperature. b) Cycling performance of the cell at 0.3 mA cm^{-2} at room temperature. The area loading is about 1.0 mAh cm^{-2}.

cycle. The irreversible capacity in the first cycle could be resulted from the side reaction between LPS and LCO cathode. The capacity remains at 101.6 mAh g^{-1} after the 50 cycles. The success of the Li/LCO cell indicates that stable Li_3N–LiF layer is a feasible strategy to suppress dendrite propagation in Li metal ASSBs.

Li dendrites form in an SSE when the driving force for Li plating in SSE is higher than the suppression capability. The low Li plating overpotential can be achieved by reducing the ASR of SSE and slightly increasing the electronic conductivity of the coating layer, while the high dendrite suppression capability can be achieved by increasing the interface energy of SSE against Li. Li dendrite growth into LPS is mainly attributed to the low interphase energy of reduced products of Li_2S and Li_3P, and the high electronic conductivity of Li_3P. Guided by the Li dendrite formation mechanism, cold-pressed Li_3N–LiF electrolytes that have a low ASR after activation process, high interface energy with Li, and a low electronic conductivity was designed to suppress Li dendrite formation. The pores in Li_3N–LiF near Li metal serve as Li reservoir enhances the interfacial contact. The Li_3N–LiF electrolytes demonstrate a high room temperature critical current density of >6 mA cm^{-2} and 6 mAh cm^{-2} capacity. Surface characteristics such SEM, XPS, and ToF-SIMS confirmed the high stability of Li_3N–LiF against Li metal.

Experimental Section

Synthesis: Li chips were purchased from MTI Corporation (250 µm). Li_3N–LiF power was obtained by high-energy mechanical milling. Li_3N (99.5%, Sigma-Aldrich) and LiF (99.99%, Sigma-Aldrich) with the molar ratio of 3:1 were used as starting materials. These materials were subjected to a zirconia ceramic vial, and ball-milled (PM 100, Retsch) at 500 rpm for 72 h in argon-filled atmosphere. PTFE was added to the prepared powered to enhance the cold-deformability (1% weight ratio). The LPS was synthesized by ball-milling the Li_2S (99.98%, Sigma-Aldrich), P_2S_5 (99%, Sigma-Aldrich) in a zirconia ceramic vial using the same method as the authors' previous work.[10]

Characterization: The morphologies of the sample were examined using a Hitachi SU-70 field-emission SEM. XPS was conducted on a high sensitivity Kratos AXIS 165 X-ray photoelectron spectrometer using Mg Kα radiation. All binding energy values were referenced to the C 1s peak at 284.6 eV. The CasaXPS software was used to fit the whole XPS spectra to get the content of different species. ToF-SIMS attached with the Ga^+ focused-ion-beam (FIB)/SEM (Tescan GAIA3) was used to analyze the distribution of lithium element in different depth of the cycled Li_3N–LiF layer. The accelerated voltage for FIB/SEM was 20 kV. Powder XRD results were obtained with a D8 Advance with LynxEye ans SolC (Bruker, USA) using Cu Kα radiation.

Electrochemistry: To assemble the Li/electrolyte/Li all-solid cell, 100 mg LPS solid electrolyte powder was pressed into a pellet under 360 MPa in a PTFE tank with a diameter of 10 mm. After that, 50 mg Li_3N–LiF solid electrolyte powder was put on both sides of the solid electrolyte and then pressed into a pellet. And then, two Li discs with a diameter of 10 mm were attached on both sides of the solid electrolyte. The formed Li/Li_3N–LiF/LPS/Li_3N–LiF/Li cell was then sandwiched and pressed under 120 MPa between two stainless-steel rods which function as current collector. For the Li/electrolyte/stainless-steel cell, only one Li disc was attached to one side of the solid electrolyte. For the assembly of the Li/Li_3N–LiF/LPS/LCO all-solid-state full cells, $LiNbO_3$-coated $LiCoO_2$ (LNO@LCO) was mixed with LPS with the weight ratio of 70:30. For the EIS test of the Li/electrolyte/Li cell was tested on Gamry workstation (Gamry 1000E, Gamry Instruments, USA) in a frequency range from 1 MHz to 0.1 Hz. The galvanostatic cycling test was determined by a Land test system (CT2001A, Wuhan, China).

DFT Calculations: First-principles calculations based on DFT[33,34] were performed using the Vienna Ab initio Simulation Package (VASP).[35] The Projector Augmented Wave[36] method with an energy cut-off of 520 eV was used to describe the ion–electron interaction on a well-converged *k*-point mesh. The Perdew–Burke–Ernzerhof functional in the generalized gradient approximation[37] was employed to calculate the exchange-correlation energy. The geometry optimizations were performed using the conjugated gradient method, and the convergence threshold was set to be 10^{-5} eV in energy and 0.01 eV $Å^{-1}$ in force. The DOS and HSE06 bandgap was calculated by PWmat code.[38] For the defect formation energy calculations, same method as Swift's work[27] was used with the help of PYMATGEN[39] and PyCDT[40] codes. The visualization of the structures was made by using VESTA.[41]

Supporting Information

Supporting Information is available from the Wiley Online Library or from the author.

Acknowledgements

This work was supported by Department of Energy (DOE) under Award number DEEE0008856.

Conflict of Interest

The authors declare no conflict of interest.

Author Contributions

X.J., S.H., and X.F. designed the experiments and analyzed data. X.J., X.H., N.P., and X.F. conducted the electrochemical experiments. X.J. conducted the calculations. X.J., P.W., and J.C. performed XRD, XPS, and ToF-SIMS. X.J. wrote the draft manuscript. All authors revised the manuscript. C.W. conceived and supervised the project. All authors contributed to the interpretation of the results.

Keywords

dendrite-free criteria, density functional theory calculations, interface energy, lithium–metal batteries, solid-state electrolytes

Received: April 22, 2020
Revised: August 14, 2020
Published online:

[1] Z. Yang, J. Zhang, M. C. Kintner-Meyer, X. Lu, D. Choi, J. P. Lemmon, J. Liu, *Chem. Rev.* **2011**, *111*, 3577.
[2] J. Janek, W. G. Zeier, *Energy* **2016**, *500*, 300.
[3] T. Famprikis, P. Canepa, J. A. Dawson, M. S. Islam, C. Masquelier, *Nat. Mater.* **2019**, *18*, 1278.
[4] A. Manthiram, X. Yu, S. Wang, *Nat. Rev. Mater.* **2017**, *2*, 16103.
[5] C. Monroe, J. Newman, *J. Electrochem. Soc.* **2005**, *152*, A396.
[6] C. Brissot, M. Rosso, J.-N. Chazalviel, S. Lascaud, *J. Power Sources* **1999**, *81-82*, 925.
[7] M. Nagao, A. Hayashi, M. Tatsumisago, T. Kanetsuku, T. Tsuda, S. Kuwabata, *Phys. Chem. Chem. Phys.* **2013**, *15*, 18600.

[8] Y. Ren, Y. Shen, Y. Lin, C.-W. Nan, *Electrochem. Commun.* **2015**, *57*, 27.
[9] T. Swamy, R. Park, B. W. Sheldon, D. Rettenwander, L. Porz, S. Berendts, R. Uecker, W. C. Carter, Y.-M. Chiang, *J. Electrochem. Soc.* **2018**, *165*, A3648.
[10] X. Fan, X. Ji, F. Han, J. Yue, J. Chen, L. Chen, T. Deng, J. Jiang, C. Wang, *Sci. Adv.* **2018**, *4*, eaau9245.
[11] E. J. Cheng, A. Sharafi, J. Sakamoto, *Electrochim. Acta* **2017**, *223*, 85.
[12] L. C. Zhang, J. F. Yang, C. L. Li, Y. X. Gao, X. P. Wang, Q. F. Fang, *J. Power Sources* **2020**, *449*, 227610.
[13] H. Liu, X.-B. Cheng, J.-Q. Huang, H. Yuan, Y. Lu, C. Yan, G.-L. Zhu, R. Xu, C.-Z. Zhao, L.-P. Hou, C. He, S. Kaskel, Q. Zhang, *ACS Energy Lett.* **2020**, *5*, 833.
[14] F. Shen, M. B. Dixit, X. Xiao, K. B. Hatzell, *ACS Energy Lett.* **2018**, *3*, 1056.
[15] T. Swamy, R. Park, B. W. Sheldon, D. Rettenwander, L. Porz, S. Berendts, R. Uecker, W. C. Carter, Y.-M. Chiang, *J. Electrochem. Soc.* **2018**, *165*, A3648.
[16] C.-L. Tsai, V. Roddatis, C. V. Chandran, Q. Ma, S. Uhlenbruck, M. Bram, P. Heitjans, O. Guillon, *ACS Appl. Mater. Interfaces* **2016**, *8*, 10617.
[17] X. Han, Y. Gong, K. K. Fu, X. He, G. T. Hitz, J. Dai, A. Pearse, B. Liu, H. Wang, G. Rubloff, *Nat. Mater.* **2017**, *16*, 572.
[18] C. Wang, Y. Gong, B. Liu, K. Fu, Y. Yao, E. Hitz, Y. Li, J. Dai, S. Xu, W. Luo, *Nano Lett.* **2017**, *17*, 565.
[19] W. Luo, Y. Gong, Y. Zhu, Y. Li, Y. Yao, Y. Zhang, K. Fu, G. Pastel, C. F. Lin, Y. Mo, *Adv. Mater.* **2017**, *29*, 1606042.
[20] H. Xu, Y. Li, A. Zhou, N. Wu, S. Xin, Z. Li, J. B. Goodenough, *Nano Lett.* **2018**, *18*, 7414.
[21] A. Sharafi, E. Kazyak, A. L. Davis, S. Yu, T. Thompson, D. J. Siegel, N. P. Dasgupta, J. Sakamoto, *Chem. Mater.* **2017**, *29*, 7961.
[22] Y. Chen, Z. Wang, X. Li, X. Yao, C. Wang, Y. Li, W. Xue, D. Yu, S. Y. Kim, F. Yang, A. Kushima, G. Zhang, H. Huang, N. Wu, Y.-W. Mai, J. B. Goodenough, J. Li, *Nature* **2020**, *578*, 251.
[23] J. Kasemchainan, S. Zekoll, D. Spencer Jolly, Z. Ning, G. O. Hartley, J. Marrow, P. G. Bruce, *Nat. Mater.* **2019**, *18*, 1105.
[24] X. Fan, X. Ji, L. Chen, J. Chen, T. Deng, F. Han, J. Yue, N. Piao, R. Wang, X. Zhou, X. Xiao, L. Chen, C. Wang, *Nat. Energy* **2019**, *4*, 882.
[25] X. Fan, L. Chen, O. Borodin, X. Ji, J. Chen, S. Hou, T. Deng, J. Zheng, C. Yang, S.-C. Liou, K. Amine, K. Xu, C. Wang, *Nat. Nanotechnol.* **2018**, *13*, 715.
[26] X. Cao, X. Ren, L. Zou, M. H. Engelhard, W. Huang, H. Wang, B. E. Matthews, H. Lee, C. Niu, B. W. Arey, Y. Cui, C. Wang, J. Xiao, J. Liu, W. Xu, J.-G. Zhang, *Nat. Energy* **2019**, *4*, 796.
[27] M. W. Swift, Y. Qi, *Phys. Rev. Lett.* **2019**, *122*, 167701.
[28] F. Han, Y. Zhu, X. He, Y. Mo, C. Wang, *Adv. Energy Mater.* **2016**, *6*, 1501590.
[29] U. Alpen, *J. Solid State Chem.* **1979**, *29*, 379.
[30] R. Garcia-Mendez, F. Mizuno, R. Zhang, T. S. Arthur, J. Sakamoto, *Electrochim. Acta* **2017**, *237*, 144.
[31] A. Kato, H. Kowada, M. Deguchi, C. Hotehama, A. Hayashi, M. Tatsumisago, *Solid State Ionics* **2018**, *322*, 1.
[32] Y.-G. Lee, S. Fujiki, C. Jung, N. Suzuki, N. Yashiro, R. Omoda, D.-S. Ko, T. Shiratsuchi, T. Sugimoto, S. Ryu, J. H. Ku, T. Watanabe, Y. Park, Y. Aihara, D. Im, I. T. Han, *Nat. Energy* **2020**, *5*, 299.
[33] P. Hohenberg, W. Kohn, *Phys. Rev.* **1964**, *136*, B864.
[34] W. Kohn, L. J. Sham, *Phys. Rev.* **1965**, *140*, A1133.
[35] G. Kresse, J. Hafner, *Phys. Rev. B* **1994**, *49*, 14251.
[36] P. E. Blöchl, *Phys. Rev. B* **1994**, *50*, 17953.
[37] J. P. Perdew, K. Burke, M. Ernzerhof, *Phys. Rev. Lett.* **1996**, *77*, 3865.
[38] W. Jia, Z. Cao, L. Wang, J. Fu, X. Chi, W. Gao, L.-W. Wang, *Comput. Phys. Commun.* **2013**, *184*, 9.
[39] S. P. Ong, W. D. Richards, A. Jain, G. Hautier, M. Kocher, S. Cholia, D. Gunter, V. L. Chevrier, K. A. Persson, G. Ceder, *Comput. Mater. Sci.* **2013**, *68*, 314.
[40] D. Broberg, B. Medasani, N. E. Zimmermann, G. Yu, A. Canning, M. Haranczyk, M. Asta, G. Hautier, *Comput. Phys. Commun.* **2018**, *226*, 165.
[41] K. Momma, F. Izumi, *J. Appl. Crystallogr.* **2011**, *44*, 1272.